Exp Fluids (2012) 52:1373–1387
DOI 10.1007/s00348-011-1252-6

RESEARCH ARTICLE

Wind tunnel measurements of the preferential concentration of inertial droplets in homogeneous isotropic turbulence

Colin P. Bateson · Alberto Aliseda

Received: 24 May 2011 / Revised: 18 October 2011 / Accepted: 8 December 2011 / Published online: 13 January 2012

Abstract We describe an experimental setup aimed at studying turbulent-induced droplet collisions in a laboratory setting. Our goal is to reproduce conditions relevant to warm-rain formation in clouds. In these conditions, the trajectories of small inertial droplets are strongly influenced by the background air turbulence, and collisions can potentially explain the droplet growth rates and spectrum broadening observed in this type of clouds. Warm-rain formation is currently under strong scrutiny because it is an important source of uncertainty in atmospheric models. A grid at the entrance of a horizontal wind tunnel produces homogeneous isotropic turbulence at a Re_λ in the range of 400–500. Water droplets are injected from the nodes of the turbulence-inducing grid at a volume fraction (ϕ) of 2.7×10^{-5} and with sizes of 10–200 μm. A complex manifold-injection system was developed to obtain uniform water droplet seeding, in terms of both water content and size distribution. We characterize the resulting droplet-laden turbulent flow, and the statistics of droplet pairs are measured and analyzed. We found that the radial distribution function (RDF), a measure of preferential concentration of droplets that plays a key role in collision kernel models, has a large peak at distances below the Kolmogorov microscale of the turbulence. At very long separations, comparable with the integral length scale of the turbulence, these RDFs show a slow decay to the average probability given by the mean droplet number density. Consistent with this result, conditional analysis shows an increased local concentration of droplets within the inertial length scale ($\approx$ 10–100 Kolmogorov lengths). These results are in good agreement with previous experiments that found clustering of inertial droplets with $St \approx 1$ at scales on the order of 10η. Ultimately, our results support the hypothesis that turbulence-induced preferential concentration and enhanced settling can lead to significant increases in the collision probability for inertial droplets in the range 10–50 μm.

C. P. Bateson (✉) · A. Aliseda
Department of Mechanical Engineering,
University of Washington, 4000 15th Ave NE, Box 352600,
Seattle, WA 98195-2600, USA
e-mail: cbateson@u.washington.edu

A. Aliseda
e-mail: aaliseda@u.washington.edu

1 Introduction

Turbulent coagulation is an important mechanism for particle growth in many engineering and environmental processes (Wang et al. 2000). Examples include cyclonic particle separation (Wang et al. 2006a; Yaxin and Su 2006), spray atomization in fuel injectors (Faeth et al. 1995; Ruger et al. 2000) and liquid film coatings, and rain formation in clouds (Shaw 2003; Seifert and Beheng 2006). The inertia of the particles, or droplets, causes them to deviate from the trajectories of flow tracers, giving rise to a rich set of behaviors during which the interaction of the droplets' inertia with the turbulence in the carrier flow dominates the dynamics of the droplets.

Heavy droplets accumulate in the periphery of vortices. The droplets' inertia centrifuges them away from regions of high vorticity into regions of high strain between eddies (Maxey and Corrsin 1986; Squires and Eaton 1991). Under the influence of gravity, preferential accumulation is enhanced by the crossing trajectories effect (Wells and Stock 1983). The relative velocity between the particles and the mean flow breaks the symmetry of the interactions with the eddies and results in the particles being

preferentially accumulated in the downward side of the eddies—a phenomenon commonly referred to as preferential sweeping (Maxey 1987). The coupling of the inertial accumulation and the gravitational bias in the interaction of heavy particles with turbulent eddies enhances the preferential accumulation effect, leading to a higher concentration and an even higher settling velocity of the particles (Wang and Maxey 1993). The particles in areas of high concentration interact through short-range aerodynamic perturbations that lead to collective dynamics of these particle clusters. In particular, those particles that form part of a cluster have an increased settling velocity. This velocity is a many-fold increase over their Stokes velocity and even over their turbulence-enhanced settling in isolation (Aliseda et al. 2002).

All of these phenomena affecting inertial particles in turbulence result in a significant increase in local particle concentration and interparticle relative velocity. Both of these physical variables play an important role in the particle collision kernel (Eq. 1) and therefore increase the probability of collision-coalescence (Wang et al. 2005). The study of these fundamental multiphase flow phenomena has formed the foundation of the leading hypothesis for explaining the growth rate of droplets in clouds during the process of warm-rain formation.

The atmospheric science community has long tried to formulate a model that correctly captures the physics of the warm-rain process. Condensational growth produces a narrow size spectrum as growth rate is inversely proportional to the surface-to-volume ratio. Condensation is also inefficient to grow droplets larger than 10 μm: it would take hours for drops to grow from 10 to 100 μm by condensation alone (Jonas 1996), but observations have shown that drops of this size are present only 15–30 min after drop nucleation (Rogers and Yau 1989). Real cloud spectra are broad and contain non-precipitating drops that are too large to be the result of condensation alone. Once formed, drops over 100 μm in diameter have significant settling velocity, and their continued growth is the result of gravity-induced collisions with smaller droplets. These two processes for droplet growth—condensation and gravity-induced collisions—are both well understood and can be modeled accurately. There is, however, a lapse in our understanding of what occurs between the two processes. The size range between 10 and 100 μm is known as the size gap. The primary mechanism for growth through the size gap is not well understood, and the uncertainty associated with this process is a source of inaccuracy in the current models of cloud dynamics.

Arenberg (1939) studied the influence of sinusoidal velocity fluctuations—an early model for turbulence—on the relative velocity and concentration of droplets in clouds. He determined that collisions would be enhanced by these fluctuations. East and Marshall (1954) took the work on droplet collision efficiencies by Langmuir (1948) and applied it to a model of collisions that included both random turbulent motion and gravity. They developed a model for turbulence-induced collisions that treated turbulence as an increase in the acceleration due to gravity and, as a result, missed the influence of the spatial inhomogeneity of turbulence. These works led to the seminal paper by Saffman and Turner (1956), who first predicted that turbulence enhances collision probability in two ways: first, by increasing the relative velocity associated with spatial inhomogeneity in the turbulence, and second, by increasing the relative velocity between droplets of different sizes associated with differential droplet responses to the turbulent eddies resulting from their different inertia. de Almeida (1976, 1979a) performed a battery of Monte Carlo simulations to study the increase in the geometric collision efficiency resulting from turbulence. These results were then applied to the evolution of cloud droplet size spectra (de Almeida 1979b), to find that the coalescence process was greatly enhanced by turbulence. Grover and Pruppacher (1985) argued that while de Almeida (1979b) used the wrong part of the turbulent energy spectrum for the drop sizes he considered, this only affects the quantitative applicability of those results, not their qualitative validity.

Starting from first principles, Maxey and Riley (1983) included particle inertia in the equations of motion they derived for a rigid, spherical particle in a turbulent flow. Their work has contributed significantly to the understanding of turbulent collisions by enabling researchers to use a variety of computational tools to study particle-turbulence interactions in detail. As a result, preferential concentration and preferential sweeping have been studied extensively (Squires and Eaton 1991; Wang and Maxey 1993; Eaton and Fessler 1994; Truesdell and Elghobashi 1994), and several models for their influence on droplet collisions have been formulated (Shaw et al. 1998; Vohl et al. 1999; Pinsky et al. 2006; Zaichik et al. 2006; Xue et al. 2008). Reuter et al. (1988) put forward a stochastic model of the drop-collision process in turbulent air that was based on the "over-lapping eddy" mechanism: when two eddies collide—or overlap—the droplets they are carrying may collide as well. In a follow-up paper, Reuter et al. (1989) developed a probabilistic collection kernel and used it to calculate the evolution of a cloud droplet spectrum. Sundaram and Collins (1997) were the first to apply the RDF to the cloud drop collision problem as a quantification of preferential concentration. Their equation incorporates preferential concentration into the collision frequency of a monodisperse particle population:

$$N_c = \frac{1}{2}\pi\sigma^2 n^2 g(\sigma) \int \mathbf{w} P(\mathbf{w}\,|\,\sigma)\mathrm{d}\mathbf{w} \quad (1)$$

where σ is the particle diameter, n is the particle number density, $g(\sigma)$ is the particle RDF evaluated at contact, $\mathbf{w}$ is the relative velocity, and $P(\mathbf{w}\,|\,\sigma)$ is the relative velocity Probability Density Function (PDF) conditioned on the contact distance. The contact distance is equal to the particle's diameter, or equivalently, it is equal to the separation distance between two particles at the instant of collision.

Wang et al. (2000) conducted three-dimensional (3D) direct numerical simulations (DNS) of particle-laden turbulent flows to study how relative velocity enhancements and preferential concentration contribute to the collision kernel. They confirmed that the increase in particle relative velocity due to turbulence is a result of large-scale turbulent motions (scales around the flow integral timescale, T_e). This effect is maximized when the particle inertial response time is the same order of magnitude as the flow integral timescale $(\tau_p/T_e = \mathcal{O}(1))$. The accumulation effect was found to enhance collisions by a factor of $(1 + 0.14Re_\lambda)$, and this enhancement was largest for Stokes numbers $(St = \tau_p/\tau_\kappa)$ equal to one. Wang et al. (2006b) used a Monte-Carlo approach to capture the stochastic nature of droplet growth from collision events. They showed a 40% reduction in the time for drizzle formation to occur with a turbulence dissipation rate (ε) of 400 $\mathrm{cm^2/s^3}$ as compared to the time for drizzle formation due to solely gravity-induced collisions $(\varepsilon = 0\,\mathrm{cm^2/s^3})$. Following up on this study, Ayala et al. (2008) and Wang et al. (2008) presented DNS studies of the geometric collision rates of droplets that focused specifically on a parameter range relevant to clouds $(d = 20{-}120\,\mu\mathrm{m},\ \varepsilon = 10{-}400\,\mathrm{cm^2/s^3})$. Using a hybrid DNS approach that includes a superposition of Stokeslets to account for the sub-Kolmogorov aerodynamics interactions between droplets, they calculated increased collision efficiencies due to turbulence.

In summary, studies have shown that turbulence enhances the collision kernel for cloud droplets in the following ways: (1) shear and differential acceleration increase the relative velocity between droplets; (2) preferential concentration increases the average pair statistics, like the RDF and the relative velocity, upon which the collision kernel depends (Pinsky et al. 1997; Sundaram and Collins, 1997; Wang et al. 2000; Zhou et al. 2001; Ayala et al. 2008); (3) selective changes in the settling rate increase the relative velocity between drops (Wang and Maxey 1993; Aliseda et al. 2002); and (4) turbulence increases collision efficiency (Pinsky et al. 1999, 2000; Wang et al. 2005, 2008). Many of these studies, however, were conducted outside the parameter range relevant to cloud microphysical processes (Vaillancourt and Yau 2000).

Here, we report on wind tunnel experiments aimed at improving the current understanding and quantitative modeling of the interaction between turbulence and inertial droplets. These experiments were conducted in a parameter range relevant to cloud microphysics. In Sect. 2, we describe extensively the experimental setup and measurement techniques used in our study. The characterization of the baseline flow and the droplet initial conditions is given in Sect. 3. The results from the experiment related to the RDF and preferential concentration are described and analyzed in Sect. 4. Finally, a brief summary of the conclusions from the experimental campaign conducted is presented in Sect. 5.

2 Experimental setup

We conducted our experiments in a horizontal, blow-down, low-speed wind tunnel. Water droplets were injected into nearly homogeneous and isotropic grid-generated turbulence. We used constant temperature hotwire anemometry (HWA) measurements to characterize the turbulence. Droplet measurements were taken with a Phase Doppler Particle Analyzer (PDPA) and used to calculate statistics relevant to the droplet collisions.

2.1 Description of the facility

2.1.1 The wind tunnel

The wind tunnel has an 8:1 ratio expansion section containing wire mesh and honeycomb screens that break down possible turbulent structures and eliminate the large-scale rotational motion of the air flow created by the axial compressor. The air flows into a plenum (2.25 m × 1.2 m × 1.2 m) to dampen the remaining anisotropic turbulent fluctuations. The flow at the entrance to the test section, prior to the turbulence-inducing grid, is homogeneous turbulence with $u'/U_{\mathrm{avg}} = 10\%$. At the end of the flow conditioning section, the flow goes through a dual-purpose grid: it generates homogeneous, isotropic, slowly decaying turbulence, and serves as the support for the droplet injection system. The test section is formed by acrylic panels (1.2 m × 1.2 m constant cross-section and 3 m long) to allow optical access to the flow. At the downstream end of the tunnel, a large diffuser decelerates the flow and discharges it into the atmosphere through a filter that captures the water droplets as they leave the tunnel (Fig. 1).

2.1.2 The turbulence-inducing grid

The grid used in our experiments is a 9 × 9 biplanar array formed by 1″ (2.54 cm) diameter aluminum tubes. The

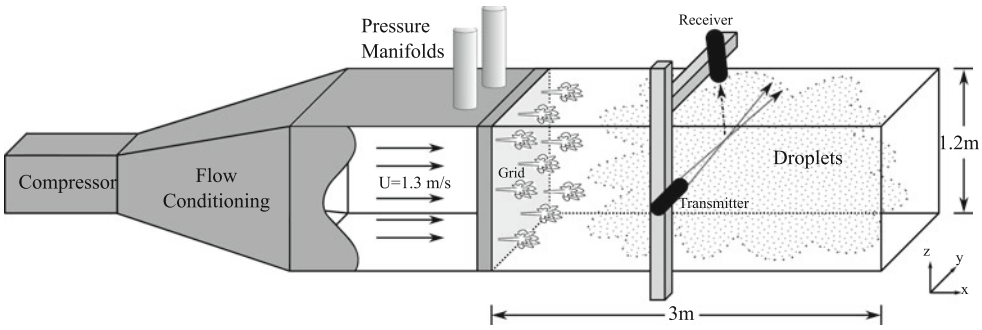

Fig. 1 An illustration of our wind tunnel experiment

water and air supply lines run inside the hollow tubes to each of the 81 droplet injectors that are integrated into the intersections of the tubes. The geometry of a turbulence-inducing grid is characterized by the diameter (d) of the grid tubes, the grid spacing (M), and the grid solidity (S). The grid spacing, defined as the distance between the center of two adjacent parallel tubes, is $4''$ (10.16 cm). The non-dimensional solidity parameter, defined as the ratio of the obstructed area to the total area of the grid, describes the degree of obstruction the grid creates in the flow. It is equal to 0.39 in our experiment. Corrsin (1963) suggested that, in order to avoid the influence of the walls on grid turbulence and ensure that an appreciable part of the tunnel satisfies the criterion for homogeneity, the ratio of the width or height (H) of the wind tunnel to the mesh size (M) should be much greater than one. For our experiment, $H/M = 11.8$. We also verified that the ratio between the gas flow rate injected by the jets and the wind tunnel flow rate is very low ($J = Q_j/Q_{wt} \approx$ 1–2%) (Gad-el Hak and Corrsin 1974).

The flow through a grid is characterized by the grid Reynolds number (Re_M), which is defined as $Re_M = \frac{U_o M}{\nu}$, where U_o is the mean free-stream velocity, ν is the kinematic viscosity, and grid mesh size (M) is the length scale. This is the same length scale used to non-dimensionalize distances behind a grid. Distances are written in terms of x/M (i.e., $x = 20M$), where x is the position along the length of the wind tunnel test section, and $x = 0$ at the grid.

The flow downstream from our grid can be divided into two regions. In the first region, the developing region, the wakes behind the grid bars are growing and interacting with each other, and the flow is inhomogeneous and anisotropic. In the second region, the initial period, the non-linear interactions between the different structures coming from the grid have given rise to a fully developed turbulence with a continuous spectrum. The resulting turbulence is nearly homogeneous, isotropic and slowly decaying. All of the measurements for our experiment were made within this region, which is known to extend from $10M$ to $150M$ downstream from the grid (Wells and Stock 1983).

2.1.3 Droplet delivery system

The droplet delivery system fills the wind tunnel test section with water droplets that resemble those found in warm-rain clouds at the onset of precipitation. At each droplet injector, the high-momentum air jet impinges on the low-momentum water jet at a large angle, atomizing the liquid and producing a very dense spray of small droplets (d = 10–200 μm). The grid was designed to equally distribute eighty-one identical atomizers across the cross-section of the wind tunnel. The injectors were installed in the grid so that the air jets exit parallel to the mean flow in the wind tunnel.

Droplet size distribution and liquid mass fraction of a spray can be controlled by the air supply pressure and the water flow rate, as shown by Lázaro and Lasheras (1992). First, the water and air are fed into pressure manifolds to ensure equal pressures (and volumetric flow rates) at each of the eighty-one injectors. Then, polyurethane tubes run from the manifolds, through holes in the top of the wind tunnel, and down inside the tubes of the grid where they are attached to the injectors. All the atomizers are connected to the manifolds with equal lengths of tubing to ensure the same pressure loss between each atomizer and each manifold. Figure 2 is a schematic of the droplet delivery system.

Due to the weight of the water column, the height difference between the top and bottom of the grid (ΔH) creates a non-negligible hydrostatic pressure head between the different injector rows. This is a problem, because in order to create a homogeneous spatial distribution of droplets in the tunnel, the flow rate to every injector must be equal. To solve this problem, we used short lengths of stainless steel microtubing installed in the manifold outlets to alter the pressure drop across the outlets in order to compensate for the hydrostatic pressure difference. A detailed description of the process used to determine the exact dimensions of the microtubes can be found in Bateson (2010). As installed, the microtubes equalize the water pressure exiting the manifold for a nominal flow rate of 1.4 LPM. Over our experiment's entire operating range

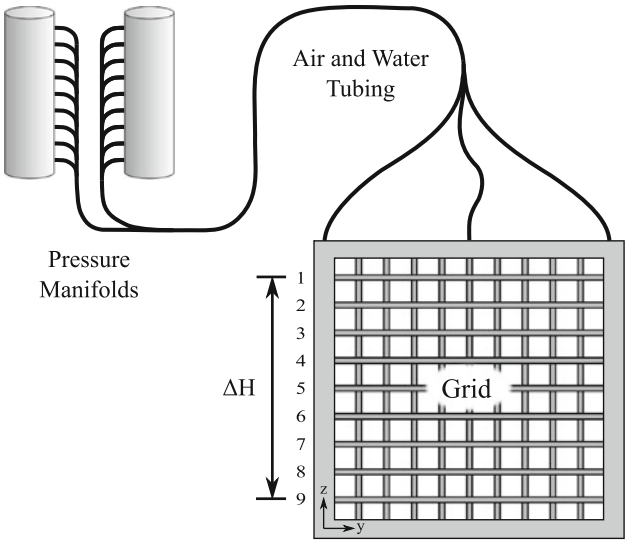

Fig. 2 An illustration of the droplet delivery system. Separate air and water pressure manifolds supply the atomizers embedded in the grid. The height difference (ΔH) between each row of atomizers creates a hydrostatic pressure head for which the water manifold has been designed to compensate

(0.8–6.0 LPM) the microtube solution results in a maximum difference in flow rate of 5% between injectors.

For the preliminary characterization of our experiment, we chose a volumetric flow rate of 3 LPM of water. This flow rate was selected as the result of a tradeoff between two competing factors that affected our PDPA data collection: (1) increasing the liquid water content increases collisions and preferential concentration; (2) the higher the volume fraction of water droplets, the faster the droplets deposit on the walls of the test section where they scatter the laser light passing into the tunnel and adversely affect the PDPA measurements. Ultimately, 3 LPM maximized the PDPA data rate during our experiments.

At 3 LPM of water and a wind tunnel flow rate of approximately 1.9 m^3/s, we produced a volume fraction of 2.7×10^{-5} in the tunnel test section, which is equivalent to a liquid water content (LWC) of 27 g/m^3. While this value is an order of magnitude higher than typical for cumulonimbus clouds, the resulting mass loading and volume fraction of water are low enough to assume that the turbulence is unaffected by the presence of the water droplets. Therefore, the analysis of our data and its implications for the behavior of inertial droplets in turbulence are applicable to cloud processes. Our high LWC facilitates the experimental characterization of the collision process by increasing the probability of collisions during the short time the droplets have to interact inside the wind tunnel. These high LWC conditions allow us to build statistics of turbulence-induced droplet collisions and measure the collisions' effect on the overall process of droplet growth within the length and timescales of a laboratory setting.

2.2 Experimental techniques

PDPA (TSI Inc., Shoreview, MN.) is a non-intrusive light interferometry system used for measuring the motion of particles (solid particles, liquid droplets or gas bubbles) immersed in fluid flows. A pair of laser beams, shifted in frequency (40 MHz) from each other by a Bragg Cell, are focused at a small incidence angle on a specific point (the probe volume) inside the particle-laden flow. Measurements of the velocity and diameter of the particles are taken by analyzing the frequency and phase shift, respectively, of the light scattered by these particles. We use large samples of these measurements to calculate statistics of both the liquid droplets and the carrier air flow. Details of PDPA measurement theory and operation can be found in Bachalo (1994), Albrecht (2003). We collected the data for the experiments and results presented here using the PDPA optical and operational settings listed in Table 1. PDPA measurements were made at five different locations—or *stations*—along the tunnel: $x/M = 6.4, 14, 17, 22, 29$. At each station, measurements were taken at the same position relative to the height (H) of the wind tunnel's square cross-section.

The PDPA receiver was positioned at a 70° angle to the direction of light propagation from the transmitter to collect forward scattered light in the first mode of diffraction, while maximizing the range of measurement positions within the wind tunnel with a fixed focal length lens (250 mm). This means that the receiver looks into the tunnel at an angle with respect to the tunnel wall (Fig. 3), which introduces a problem with the refraction of light as it propagates through the acrylic wind tunnel walls. Two triangular acrylic prisms, with a matching 70° angle between their faces, were built and attached to both sides of the top test section wall, creating a rigid body whose surfaces are perpendicular to the receiver's lens, thus minimizing the effects of light refraction through the tunnel walls. One prism sits on the top of the tunnel, and the other prism is suspended on the inside of the tunnel using magnets. A thin layer of glycerol, which has an index of refraction similar to acrylic, is used between the surfaces to minimize the light scattered at the interface between the prisms and the top tunnel wall.

For the diameter measurements based on Mie scattering, the droplets are assumed to be perfectly spherical. The Weber number for the droplets, based on the droplet

Table 1 PDPA operational settings

Setting	Value
Fringe spacing	12.865 μm
Measurement volume dimensions	0.19 × 0.19 × 0.19 mm
Sample size (each location)	75,000 drops
Range of measurable diameters	1.47–590.07 μm

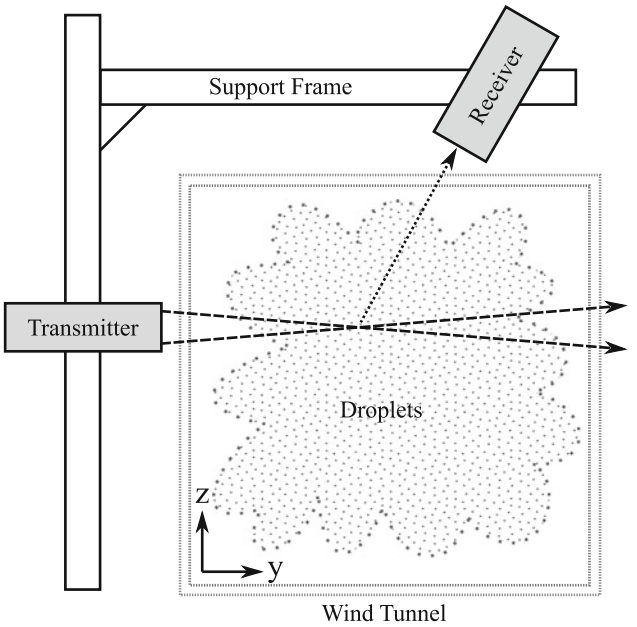

Fig. 3 This is an illustration of the PDPA system showing the relationship between the receiver and the transmitter and their orientation to the wind tunnel. The laser beams leaving the transmitter are represented by *dashed lines*, and their intersection locates the measurement volume. The *dotted line* is the light scattered by the droplets that pass through the measurement volume. Our measurements were made at the same position relative to the height (H) of the wind tunnel's square cross-section ($y/H = 0.21$, $z/H = 0.82$)

Table 2 Hotwire anemometry settings

Setting	Value
Sampling frequency	10 kHz
Number of samples	10^6
Wire diameter	54 μm
Wire length	1 mm

diameter and the turbulent velocity RMS, is on the order of 10^{-2}. Therefore, any deformations resulting from unsteady pressure forces in the flow field are quickly dominated by the restoring effects of surface tension. For this reason, we assume that the droplets remain spherical throughout the experiments.

3 Experimental characterization

In order to characterize the turbulent flow in the wind tunnel, the velocity was measured with HWA at five different cross-sectional planes downstream of the turbulence-inducing grid (Table 2). Each cross-section is described by 169 locations (a 13 × 13 mesh with 5 cm spacing) that show the central core of the wind tunnel, as well as the boundary layers growing along the walls. Since the presence of water drops in the flow would adversely affect our hotwire measurements, we conducted our velocity measurements with only air flowing through the droplet injectors. We assume that the droplet formation process does not affect the turbulence levels inside the tunnel.

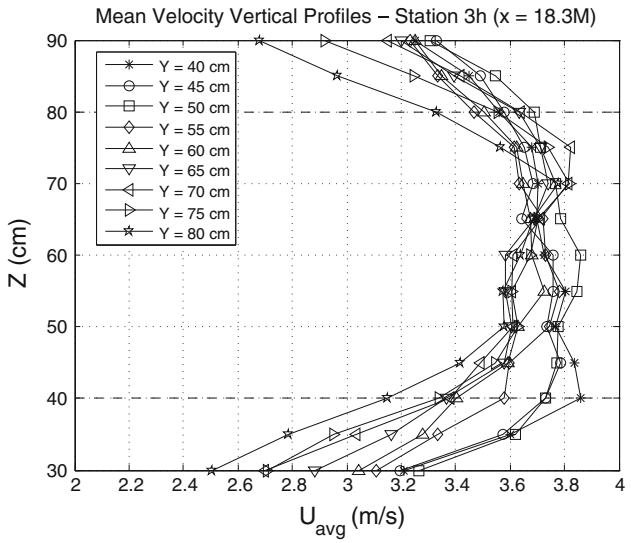

Fig. 4 Vertical profiles of the average velocity measured with a hotwire at Station 3h ($x = 18.3M$), the hotwire measurement location that most closely matches the location of PDPA Station 3 ($x = 17M$). Each data series corresponds to the velocity measurements at a single Y position and along a *vertical line* in the Z direction. The *dashed lines* represents where we defined the boundary between the core flow and the region dominated by wind tunnel walls' influence on the flow

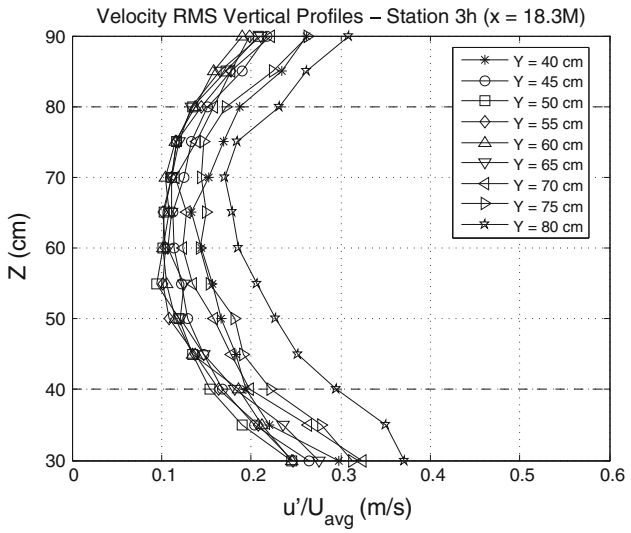

Fig. 5 Vertical profiles of the non-dimensionalized RMS velocity measured with a hotwire at Station 3h ($x = 18.3M$), the hotwire measurement location that most closely matches the location of PDPA Station 3 ($x = 17M$). Each data series corresponds to the velocity measurements at a single Y position and along a *vertical line* in the Z direction. The *dashed lines* represents where we defined the boundary between the core flow and the region dominated by the wind tunnel walls' influence on the flow

Table 3 Relevant flow parameters and scales describing the conditions inside the wind tunnel: the turbulent dissipation rate (ε); the Kolmogorov length (η_κ), time (τ_κ), and velocity (u_κ) scales; the Taylor microscale (λ); and the Reynolds number based on the Taylor microscale (Re_λ)

Station	x/M	x (m)	ε (m^2/s^3)	η_κ (μm)	τ_κ (ms)	u_κ (m/s)	λ (mm)	Re_λ
1h	6.3 ± 0.1	0.64 ± 0.01	0.75 ± 0.125	260 ± 11	4.5 ± 0.4	0.058 ± 0.002	14.0 ± 1.0	340 ± 110
2h	12.0 ± 0.1	1.22 ± 0.01	0.115 ± 0.027	410 ± 17	11.4 ± 0.9	0.036 ± 0.002	18.0 ± 0.7	410 ± 130
3h	18.3 ± 0.1	1.86 ± 0.01	0.055 ± 0.014	490 ± 22	16.5 ± 1.3	0.030 ± 0.002	22.0 ± 0.7	410 ± 90
4h	21.4 ± 0.1	2.17 ± 0.01	0.040 ± 0.023	535 ± 18	19.4 ± 0.9	0.028 ± 0.002	20.2 ± 0.6	420 ± 70
5h	27 ± 0.1	2.74 ± 0.01	0.035 ± 0.011	545 ± 9	20.7 ± 0.5	0.027 ± 0.001	19.5 ± 0.8	480 ± 80

From the hotwire data, we calculated the average streamwise velocity (U), the root mean square (RMS) of the velocity fluctuations (u'), the longitudinal 1D energy spectrum (E_{11}), the turbulent kinetic energy dissipation rate (ε), and the Kolmogorov and Taylor microscales. These turbulence statistics were analyzed to verify that the turbulence induced by the grid inside the wind tunnel's core is indeed isotropic and homogeneous. Figures 4 and 5 show the average velocity and RMS velocity profiles, respectively. The turbulence statistics obtained from the hotwire, which were used for the analysis of the droplet-laden flow, are shown in Table 3.

The two plots show the velocity data collected at Station 3h ($x = 18.3M$). Since this station is within the initial period, we expect to see homogeneous and isotropic turbulence. Each data series in the plots corresponds to the velocity measurements at a single Y position and along a vertical line in the Z direction. The dashed lines represent our definition of the boundary of the core flow region where we found homogeneous isotropic turbulence.

The average velocity in Fig. 4 varied less than 14% of the mean in the core region between $Z = Y = 40$–80 cm. The normalized velocity RMS in Fig. 5—excluding the data series at $Y = 80$ cm—ranged from 10 to 23% in this same region. The data collected at $Y = 80$ cm were included in Figs. 4 and 5 for the sake of symmetry, but they are clearly affected by the boundary layer—hence, their exclusion from our quantification of the flow's homogeneity.

We calculated the longitudinal 1D turbulent energy spectrum (E_{11}) using the velocity measurements we collected with the hotwire anemometer. Figure 6 shows E_{11} plotted as a function of frequency (ω).

Using the homogeneous and isotropic assumption, we were able to calculate the turbulent kinetic energy dissipation rate (ε) by taking the integral of the premultiplied energy spectrum:

$$\varepsilon = 15\nu \int_0^\infty k^2 E_{11}(k)\mathrm{d}k \tag{2}$$

From the dissipation rate, we computed the rest of the Kolmogorov microscales ($\eta = (\nu^3/\varepsilon)^{1/4}$, $\tau_\kappa = (\nu/\varepsilon)^{1/2}$, $u_\kappa = (\nu\varepsilon)^{1/4}$). Table 3 lists these turbulence statistics for each of the five hotwire measurement stations. These statistics are representative of the flow in the useful part of the cross-section of the wind tunnel as identified by the hotwire velocity profiles (Figs. 4, 5). The single values in Table 3 were computed from the hotwire measurements at the same location in the core region of the flow at each particular station along the length of the tunnel. The variability in these values within the cross-section at each station is reported as a plus or minus range around the single, centerline values.

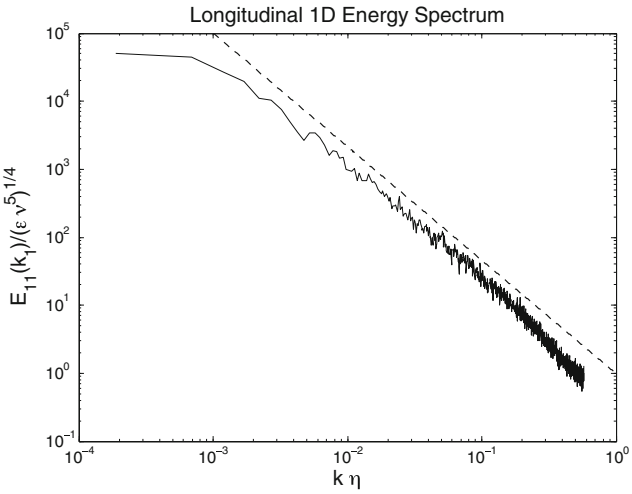

Fig. 6 Longitudinal 1D turbulent energy spectrum from hotwire measurements made at Station 3h ($x = 18.3M$). The *dashed line*, with a −5/3 slope, is included as a visual reference for the slope predicted for the inertial range of turbulent energy spectra by Kolmogorov's theory

We performed error analysis on the 1D HWA data to show both the statistical convergence of the time series and the intrinsic accuracy of the measurements. To create Figs. 7 and 8, we divided a single time series (10^6 measurements) into a varying number (N) of smaller samples and made scatter plots of the mean and RMS velocity as functions of sample size. The plots show how the variability between different samples decreases as the sample size increases. The black line in Fig. 8 shows the evolution of the mean value of the N RMS velocity samples at each

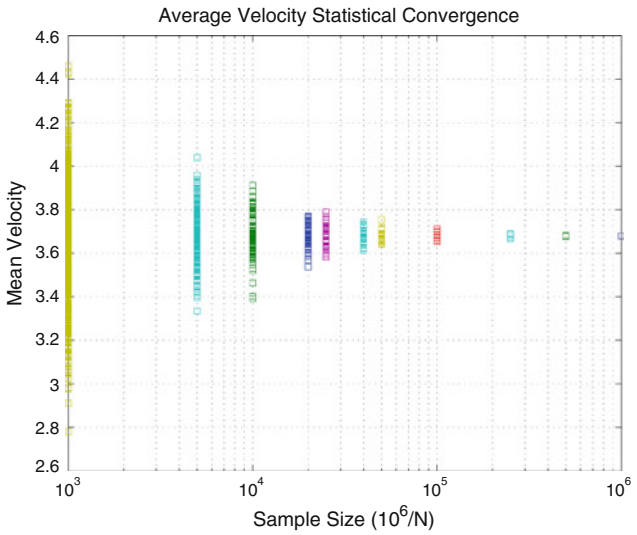

Fig. 7 The convergence of the mean velocity statistic calculated from hotwire measurements at Station 3h ($x = 18.3M$)

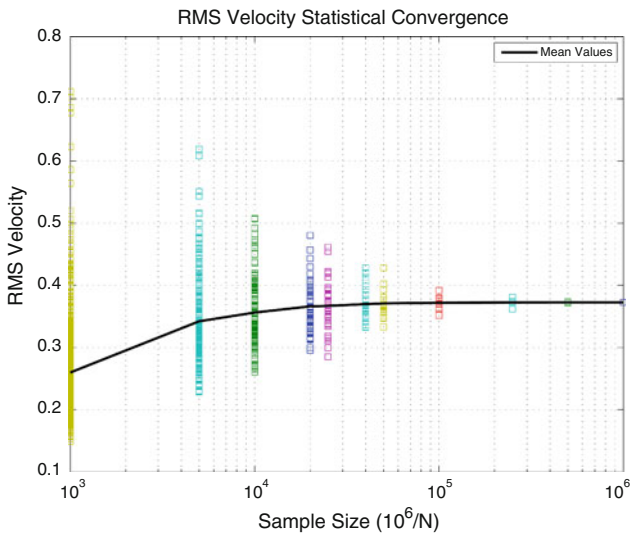

Fig. 8 The convergence of the RMS velocity statistic calculated from hotwire measurements at Station 3h ($x = 18.3M$)

sample size. At a sample size of 20,000, the RMS velocity has converged to more than 98% of the value calculated for the entire time series.

To evaluate the error in the HWA measurements, we use the evolution of the velocity RMS statistics. If a time series (x) with mean (X) and "true" variance (σ^2) is split into i independent samples (x_i), the variance in the mean calculated from N independent samples is related to the variance of the entire time series by VAR(X_N) σ^2/N (George et al. 1978).

In our measurements, when we split a single time series into 50 independent, non-overlapping samples of 20,000 velocity measurements each, we observed that the variance

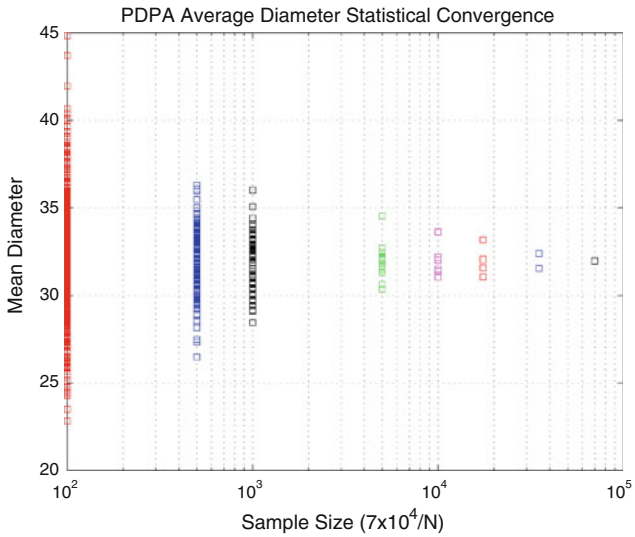

Fig. 9 The convergence of the mean droplet diameter statistic calculated from PDPA measurements

in the mean velocity asymptotes to a constant value and does not decrease like $1/N$ as predicted by the theory. We deduced that the component of the variance due to the turbulent fluctuations decays according to the theory, but the truly random error in the HWA system persists. The asymptotic value of the variance is thus the error of the HWA. On average across the core region, we found this error to be less than 5% of the full measurement.

A second source of error in our velocity measurements results from using a single component hotwire probe and ignoring the significant fluctuations in the two other components. We estimate this error to be 2% of the mean streamwise velocity for turbulence intensities of 0.2 (Goldstein 1996), which is the level of the turbulent fluctuations found in our wind tunnel.

We calibrated the HWA by making co-located hotwire and pitot tube measurements over a range of velocities. The differential pressure in the pitot tube was measured using an incline manometer, and the resultant velocities were related to corresponding hotwire voltage data using King's Law (King 1914). The uncertainty in our calibration was less than 1% across our entire velocity range. Thus, our estimate of the total error in the HWA velocity measurements is approximately 8%.

We performed the same statistical convergence analysis on a PDPA data set of 50,000 diameter measurements. We observe reasonably converged statistics for the droplet diameter measured with this technique (Figs. 9, 10). The error assessment for these diameter measurements based on Mie scattering from spherical droplets is 5% or 1.5 microns, whichever is higher.

To recreate a physical environment similar to that of clouds, we framed our experiments in the same range of the

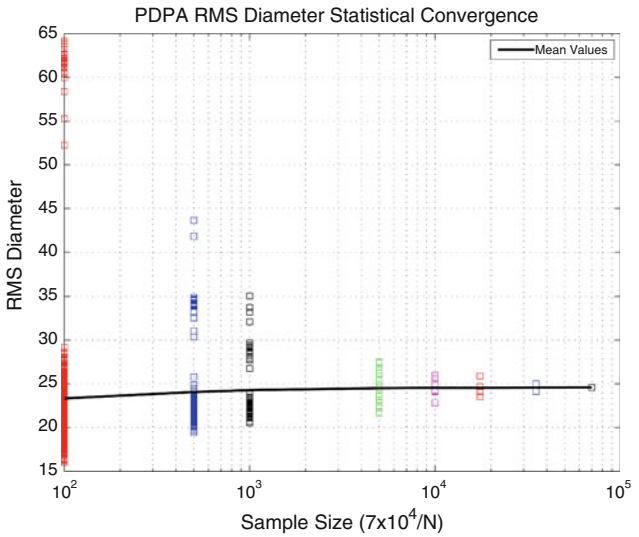

Fig. 10 The convergence of the RMS droplet diameter statistic calculated from PDPA measurements

relevant non-dimensional parameters that control droplet inertial dynamics: Stokes number, droplet terminal velocity ratio, turbulence dissipation rate, droplet volume fraction, and Re_λ. In our experiments, the dissipation rate (Table 3) and volume fraction are higher than the values found in cumulus clouds. However, since our values are the same order of magnitude as the cloud parameters, the physics of inertial droplet interactions with turbulence that we observe are still applicable to cloud processes. The Reynolds numbers in clouds cannot be recreated in the laboratory, but we conducted our experiments at a high enough value ($Re_\lambda \approx 400$) that the results are characteristic of a very high Reynolds number flow in the asymptotic Re regime.

The first purpose of the turbulence-inducing droplet injection grid is to create homogeneous and isotropic turbulence inside the wind tunnel. The second purpose is to create a homogeneous distribution of micron-sized droplets. The homogeneity of the droplet size and spatial distribution is primarily determined by the atomization conditions at the grid. After the droplets are introduced into the tunnel air flow, their distribution will quickly be modified by their interactions with the turbulence. To avoid introducing an unwanted source of inhomogeneity into the experiment, it is important that the initial droplet dispersion is homogeneous.

As described in Sect. 2.1.3, we redesigned the water manifold's tube fittings in order to equalize the pressure head available to each atomizer. The manifold design aimed to provide a homogeneous flow rate of water to each atomizer, with a maximum difference of 5%. However, there are multiple sources of uncertainty in the physical implementation of the manifold and water distribution system that could increase the inhomogeneity in water flow rates to the atomizers beyond the theoretical prediction of 5%. In order to quantify the grid's homogeneity, we conducted a simple experiment to measure the actual flow rate through each atomizer. In this experiment, we turned on the grid water supply while keeping the air supply off, so that no atomization occurred, and we captured the mass of water coming out of each injector for a constant interval of 10 s, weighing it with a high precision balance. We repeated this measurement three times to account for the variability in the collection system and the possible unsteadiness of the water injection system. For each atomizer, we averaged together the data from the three experiments. The variability intermeasurements was found to be less than 19%. The average for all the injectors, 17.27 g, was 2% higher than the theoretical value of 16.98 g. This is a good estimate of the accuracy of the model for the pressure loss in the water supply system. The standard deviation in the average values, computed for the entire grid, was 0.95 g or 6% of the mean, and the maximum deviation from the mean for a single injector was 2.14 g, or 12% of the mean (Table 4).

An equally distributed water supply does not guarantee homogeneous atomization, however. So we used the PDPA to characterize the droplet diameter and velocity close to the air/water injectors. We traversed the PDPA vertically across the sprays at two locations downstream from the grid ($x/M = 0.75$ and $x/M = 3.75$). Figure 11 shows the mean droplet velocity profiles at the two x/M locations. The high velocity jets issuing from the injectors are visible at $x/M = 0.75$. At $x/M = 3.75$, the velocity profiles are nearly uniform across both sprays showing the quick development of homogeneity. The same conclusion can be drawn from Fig. 12. This plot of the mean droplet diameter shows very small droplets near the center of the jets in the

Table 4 Statistics calculated for the grid flow rate homogeneity characterization measurements

Row	Mean (g)	Std. (g)	Deviation (%)	Max. (g)	Difference (%)
1	16.81	0.70	4.2	2.13	12.7
2	16.57	0.91	5.5	3.08	18.6
3	16.57	0.86	5.2	2.67	16.1
4	17.14	0.87	5.1	2.71	15.8
5	17.43	0.43	2.5	1.27	7.3
6	17.29	1.02	5.9	3.68	21.3
7	17.75	0.64	3.6	1.85	10.4
8	17.73	0.89	5.0	2.87	16.2
9	18.15	1.04	5.7	3.34	18.4

The values quantify the variation across each row of atomizers in both grams, and the percentage of the row's mean. By design, the atomizers in each row should have identical flow rates. The maximum difference between the mean value of any two rows was 1.6 g (9% of the mean value for the entire grid)

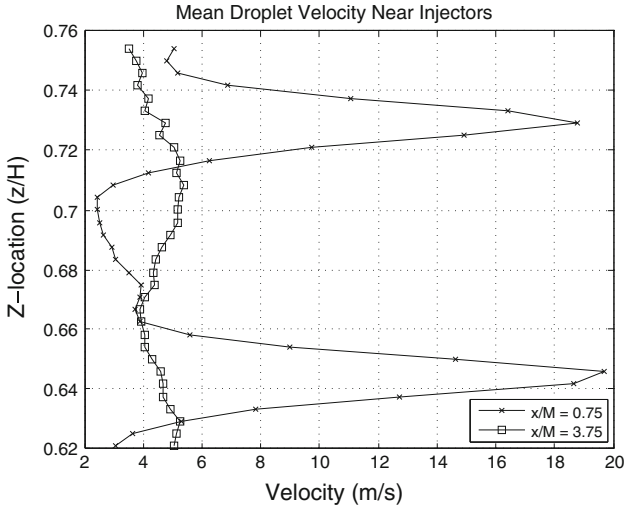

Fig. 11 Vertical profiles of mean droplet velocity from PDPA measurements at $x = 0.75M$ and $x = 3.75M$

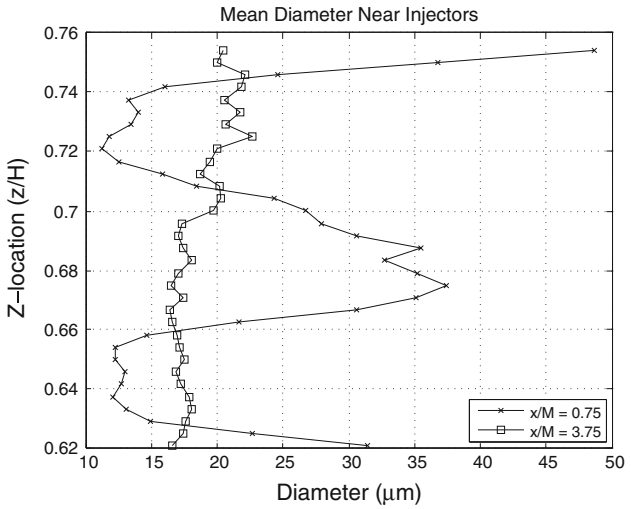

Fig. 12 Vertical profiles of mean droplet diameter from PDPA measurements at $x = 0.75M$ and $x = 3.75M$

$x/M = 0.75$ profile due to the more efficient atomization created by the high jet velocity. At $x/M = 3.75$, the mean diameter is nearly uniform across the profile. Figure 13 is a plot of all the droplet diameter PDFs calculated at each Z-location in the $x/M = 3.75$ traverse. The similarity in each of the 33 PDFs shows that the entire size distribution of the droplets becomes homogeneous very quickly. All of our results for this paper were calculated from measurements made no closer than $x/M = 14$.

Since the intent of our experimental campaign is to relate our results to the evolution of cloud droplet size spectra, it was necessary to verify that the water droplets we created had an appropriate size distribution by the time they arrived at Station 2, which is where we start taking measurements. Figure 14 shows the typical PDF of droplet

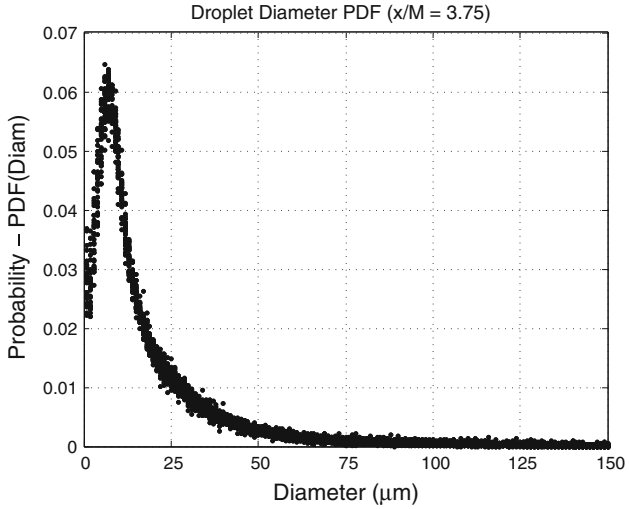

Fig. 13 The superposition of the droplet diameter PDFs calculated at each of the 33 PDPA measurement locations in the vertical traverse at $x = 3.75M$

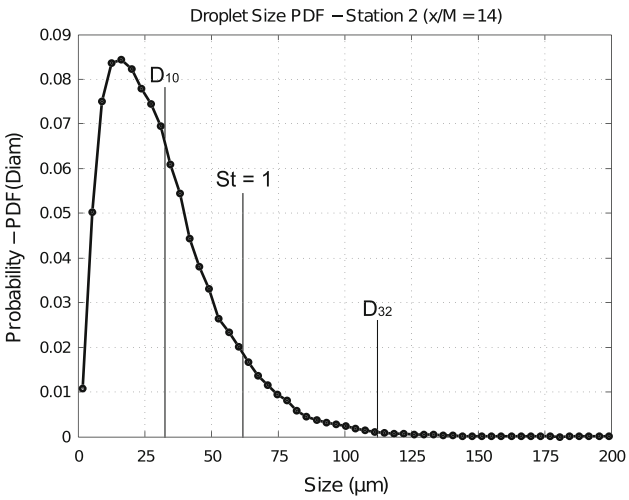

Fig. 14 Probability distribution of droplet diameters measured with the PDPA at Station 2 ($x/M = 14$, $y/H = 0.21$, $z/H = 0.82$). From *left* to *right*, the *black vertical lines* correspond to the arithmetic mean diameter (D_{10}), the diameter of a droplet with a Stokes number equal to 1, and the Sauter mean diameter (D_{32})

diameter at this location. It highlights the relative position within the distribution of the arithmetic mean diameter (D_{10}), the Sauter mean diameter (D_{32}) and the diameter corresponding to a droplet with a Stokes number of 1.

The Stokes number, defined as the ratio of a particle's viscous relaxation time (τ_p) to a turbulent timescale (τ_f) (Eq. 3), is a non-dimensional parameter that quantifies the effect of a particle's inertia on its interactions with the turbulent flow structures. We use the Kolmogorov timescale (τ_κ) as the correct turbulent timescale in this problem, following Wang and Maxey (1993). Therefore, for our analysis,

$$St = \frac{d^2 \rho_p / \rho_{\text{air}}}{18 \nu_{\text{air}}} \Big/ \left(\frac{\nu_{\text{air}}}{\varepsilon}\right)^{\frac{1}{2}} \quad (3)$$

where d is the droplet's diameter, ρ_p is the droplet's density, ρ_{air} is the density of air, ν_{air} is the kinematic viscosity of air, and ε is the turbulent kinetic energy dissipation rate in the air flow.

Since the diameter corresponding to a droplet with a Stokes number of 1 is well within the range of the droplet sizes in the flow, it is clear that droplet inertia will be the key parameter that determines how they will interact with the carrier flow turbulence. The influence of turbulence and inertia on droplet collisions can then be studied in our experiment. The typical value of the Kolmogorov length scale (η_κ) is 400 μm (See Table 3), which is much larger than the size of our droplets. The theoretical background we use in our analysis (Maxey and Riley, 1983) is justified by the limit $d/\eta \ll 1$. This, combined with the fact that the Reynolds number for our droplets based on diameter and droplet settling velocity ranges from $Re \ll 1$ to $Re \approx 1$, both support the formulation of the Stokes number in terms of the Kolmogorov timescale and the particle relaxation time based on Stokes flow.

In clouds, droplet size spectra exhibit wide variation due to the large range of conditions that occur in nature. It is worthwhile to note that the size distribution in our experiment exhibits the important general characteristics of the spectrum of a nearly precipitating cloud. The majority of the droplets in our experiment have diameters under 30 microns, which is comparable with cloud droplets. A second characteristic that our size spectrum shares with cloud droplet size spectra is a narrow distribution centered around 20 μm that, in clouds, is the result of the cloud droplets' condensational growth mechanism. Additionally, the tail in our spectrum has large diameter droplets that correspond to the few collector drops that are necessary for rain formation. This tail in our spectrum allows us to simultaneously study the collisions between cloud droplets (<60 μm) as well as between collector-sized drops (>100 μm) and cloud droplets within the same experiment.

4 Results

4.1 Conditional analysis

We performed conditional analysis on the PDPA droplet diameter data at Stations 2–4 to look at the relationship between local concentration and droplet size. Since droplets with $St \approx 1$ have been shown to preferentially concentrate most readily, we expected to find that the larger droplet clusters in our flow were comprised of droplets with Stokes numbers close to one.

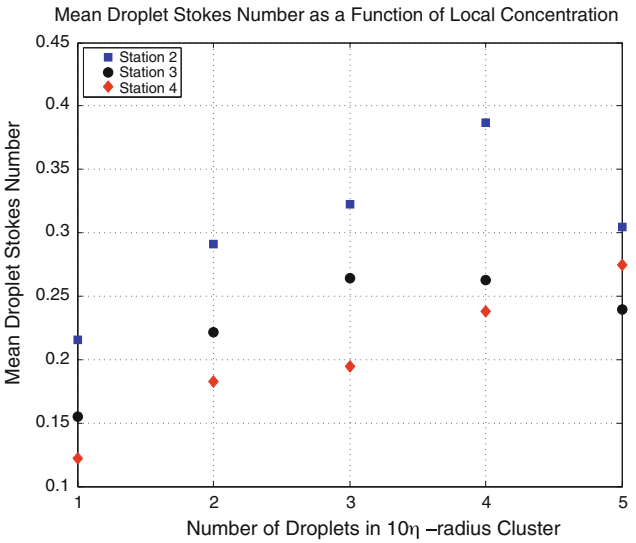

Fig. 15 Averaged droplet diameter from PDPA measurements, shown in non-dimensional form as the Stokes number, conditioned on the local number density of droplets

To test this idea, we analyzed each droplet in the data set and counted the number of neighboring drops within a 10η-long region on either side. We sorted the droplet data into groups according to each droplet's number of neighbors and calculated the mean droplet diameter in each group. Figure 15 shows the result of this analysis.

At all three measurement stations, there is a definite trend in the droplet Stokes number in relation to the local concentration. Larger clusters are made up of droplets with Stokes numbers closer to 1, as we would expect. This trend becomes noisy for clusters with five or more measured droplets because of the low number of realizations used to calculate this statistic. It is important to note again that our PDPA measurements are essentially 1D samples of a three-dimensional flow, and therefore, five droplets in close proximity along a straight line suggest a 3D cluster of hundreds of droplets. This conditional analysis shows that the droplets in our experiment tend to cluster preferentially depending on their Stokes number.

4.2 Radial distribution functions

The RDF is a distribution function of the probability that a pair of droplets will be a certain distance apart. Alternatively, the RDF measures the probability of finding a droplet in a spherical shell of thickness dr and radius r, centered on the position of another droplet. As such, the RDF is used to quantify the preferential concentration of droplets resulting from their interaction with turbulence. The droplet collision rate (Eq. 1) is directly proportional to the RDF when it is evaluated at contact, that is, at a separation distance equal to the sum of the radii of the colliding drops (Sundaram and Collins 1997).

The RDF is a three-dimensional function by definition, but due to experimental limitations, we compute a 1D RDF. By assuming our experiment is statistically stationary, and employing Taylor's hypothesis of frozen turbulence (Taylor 1938), we use the mean convective velocity to convert the temporal information from droplet arrival-time measurements to a position along a line oriented in the direction of the flow. From this position information, we can calculate the probability that two droplets are separated by some distance along this line. The 1D RDF is the distribution of that probability as a function of the separation distance. Taylor's hypothesis allows us to convert point measurements collected over time into spatial information about the structure of the turbulent fluctuations for homogeneous, shearless, grid turbulence at $u'/U_{\text{avg}} \ll 1$ (Pope 2006). In the center of our wind tunnel, u'/U_{avg} was always less than 0.2. It has been shown from theoretical analysis (Lumley 1965) that, for a turbulence intensity of 0.2, Taylor's hypothesis introduces an error of approximately 20% to the turbulent dissipation rate and less than 5% to the Kolmogorov scales.

Holtzer and Collins (2002) derived relationships between 3D RDFs and the lower-dimensional RDFs normally obtained from experimental measurements. One of these relationships can be used to compare the 1D RDFs from our experiments to 3D RDFs from DNS that have been published in the literature. These comparisons are valuable because DNS results are based on equations that either neglect aerodynamic interactions (a limiting assumption for droplets in close proximity to one another) or use simplified models to account for these sub-Kolmogorov range interactions between droplets, such as Stokeslets centered around each droplet. The results from our experiment are aimed at evaluating the effect of aerodynamic interactions in droplet dynamics at or near collision conditions and at validating the existing models used to account for these interactions in DNS simulations.

To determine the 1D RDF, we calculated the number of droplets found at increasing radial distances from the location of a central droplet. This process was repeated with each droplet in the data set serving as the central droplet, and the results were averaged and normalized with the total number of droplet pairs found within the sample. The result is a large set of data that characterizes the separation distances between all the possible droplet pairs within a certain maximum distance at which the statistics lose their physical meaning. At that larger separation distance, we expect that a spatial correlation no longer exists between two droplets. Physically, this would occur when the separation distance between particles is larger than any scale of the turbulence. To present the RDF data, we created a histogram of these separation distances. In three dimensions, the width of the histogram bins would correspond to the thickness of the spherical shell surrounding the central particle. In one dimension, the length of the sampling shell and the size of the histogram bins are identical.

Figures 16, 17, 18 show the RDFs at three places along the length of the wind tunnel ($x = 14M$, $17M$, and $22M$) calculated out to 30η. If the droplets in our flow were separated by a perfectly random distribution of distances (Poisson distribution), then the RDF would be equal to 1 everywhere. Our RDFs are much greater than 1 at small separation distances indicating that the droplets accumulate in close proximity to one another due to the turbulence. The length scale of this accumulation relates to the Kolmogorov scale of the carrier flow, but extends down to separations on the order of the diameter of the droplets. This is the key result that links preferential concentration of droplets by turbulence to the collision kernel: the droplet RDF—a measure of the preferential concentration of droplets that the collision kernel is directly proportional to—has a large peak at a spacing below the Kolmogorov scale (η). With this, we extend previous results of inertial droplet clustering at scales around 10η to much larger Re_λ and lower turbulent dissipation rates—a parameter range more representative of cloud conditions. We found that the RDF does not decay to a value of 1 until calculated for separations on the order of the integral length scale (approximately $2{,}000\eta$) at this Reynolds number (Fig. 19). This is consistent with the view that preferential accumulation for a polydisperse particle population occurs throughout the inertial range, with the purely random spatial distribution being recovered only at very large scales that integrate over lengths larger than any correlation length of the turbulence.

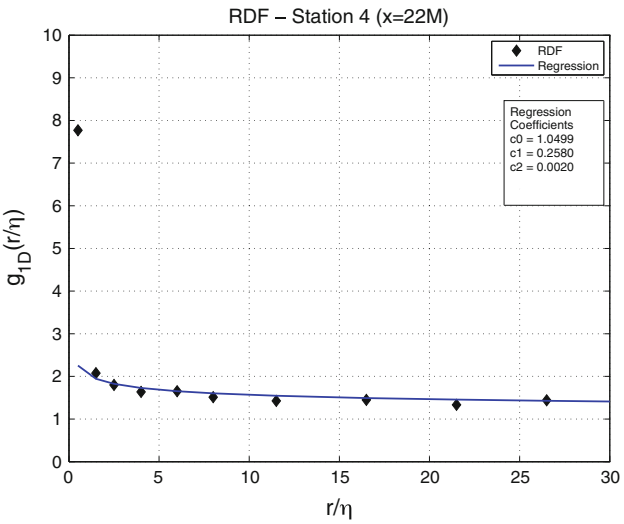

Fig. 16 The RDF at Station 4 ($x/M = 22$) and the regression to Eq. 4 shown at small separations. The RDF was calculated from PDPA measurements

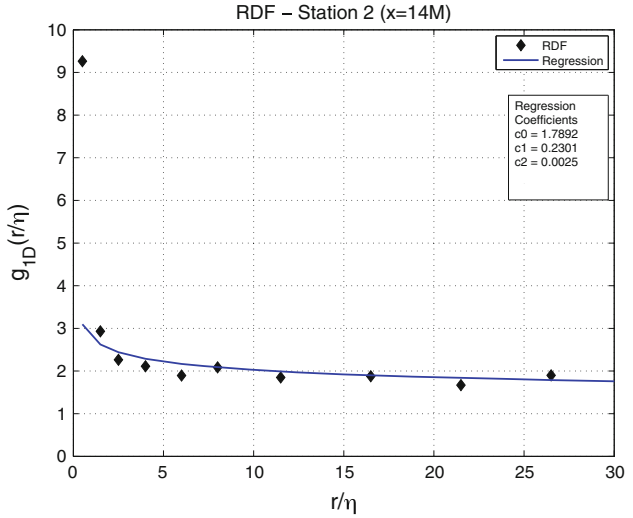

Fig. 17 The RDF at Station 2 ($x/M = 14$) and the regression to Eq. 4 shown at small separations. The RDF was calculated from PDPA measurements

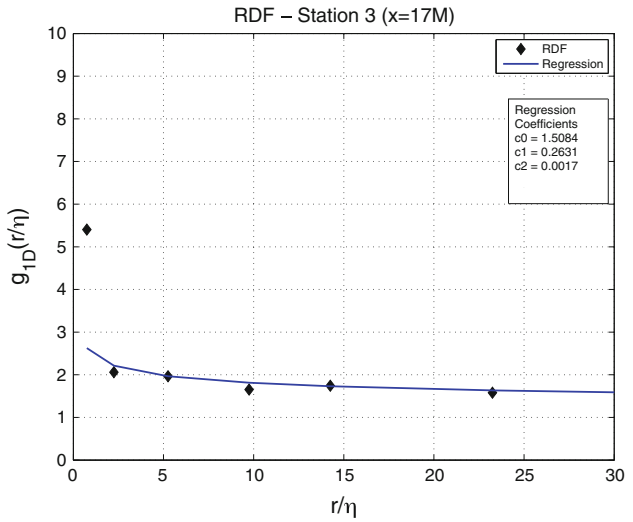

Fig. 18 The RDF at Station 3 ($x/M = 17$) and the regression to Eq. 4 shown at small separations. The RDF was calculated from PDPA measurements

The fact that the PDPA's probe has a finite cross-section defines the width of the line of fluid that is measured as it passes through this cross-section. This size-limitation introduces a distortion in the RDF computed for very small separations (comparable with the dimensions of the probe volume). As a result, we cannot resolve the RDF at separation distances smaller than 0.19 mm or about 0.5η based on the Kolmogorov length scale at Station 2 ($x/M = 14$). For this reason, the smallest separation we resolve when calculating the RDF is 1η.

For the sake of comparison, and to provide quantitative information that can be used to validate other studies, we fit

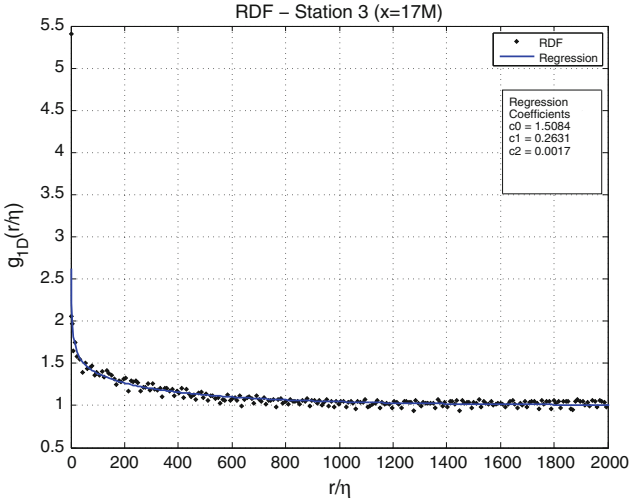

Fig. 19 The full 1D RDF ($g_{1D}(r/\eta)$) at Station 3 ($x/M = 17$) plotted as a function of the separation distance normalized by the Kolmogorov length scale. The *solid line* shows the regression to Eq. 4. Both were calculated out to $2{,}000\eta$ to show the complete decorrelation of droplet separation distance. The RDF was calculated from PDPA measurements

our data to an equation for the RDF (Reade and Collins 2000):

$$g(\hat{r}; St) = 1 + c_0 \hat{r}^{-c_1} \exp[-c_2 \hat{r}], \tag{4}$$

where $g(\hat{r})$ is the RDF, $\hat{r} = r/\eta$, and c_0, c_1, and c_2 are fit coefficients. Using data from a one-way coupling DNS, Reade and Collins (2000) show that the fit coefficients are functions of Stokes number, and therefore are functions of the droplet size distribution in the polydisperse population in our experiment. Figures 17, 18, 19 show that the form of Eq. 4 fits our data well, except at the smallest separations where it under-predicts the degree of preferential concentration. This is consistent with the fact that four-way coupling, intrinsically present in our experimental data, was not considered in the development of this expression but is critical in the behavior of the droplets at these small separations distances.

Admittedly, no conclusions can be reached about the dependency of the RDF based upon only three measurements. This will be the focus of future experiments that will study the RDF evolution with droplet population residence time, turbulence intensity of the carrier flow and droplet volume fraction.

5 Summary

We report on the development of and the first results from a well-characterized wind tunnel experimental facility designed to study the interaction between turbulence and inertial droplets under conditions representative of warm

clouds. We generate homogeneous isotropic droplet-laden turbulence at high Reynolds numbers and high droplet volume fractions. Small inertial droplets with average diameters around 20 μm (corresponding to the critical value of the size gap in warm-rain formation) are injected through two-fluid atomizers at the nodes of an active grid. The turbulence from the grid wakes and injector jets evolves to produce canonical turbulence over several meters ($10 < x/M < 30$) in the wind tunnel. Similarly, the droplets injected mix quickly to provide a uniform size and droplet number density early in the experimental test section. The resulting conditions ($Re_\lambda \approx 400$, $\varepsilon \approx 700\,\mathrm{cm^2/s^3}$, $St \approx 0.1-1$, and LWC $\approx$ 10 $\mathrm{g/m^3}$) allow us to study the influence of turbulence on the dynamics of inertial droplets, including turbulence-induced collisions, in a regime relevant to the microphysics of clouds in warm-rain conditions.

We found preferential concentration of the droplets for length scales related to the Kolmogorov scale, in good agreement with previous numerical and experimental results and consistent with our formulation of the Stokes number based on the Kolmogorov length scale. This preferential accumulation of droplets resulted in clusters with dimensions on the order of 10η, with more intense accumulation for droplets with Stokes numbers near one.

We calculate the 1D RDF to show the preferential accumulation at length scales shorter than the Kolmogorov length scale, close to the diameter of the droplets. This is relevant to the problem of turbulence-induced collisions because the RDF evaluated at contact between two droplets is an integral element in the collision kernel used to calculate the probability of these events. The 1D RDFs in our experiments show very large probabilities for droplet pairs at separations smaller than the Kolmogorov scale. The overall values are well predicted by an exponential decay law from the literature, but the actual values at the closest separations are underpredicted, presumably due to the importance of four-way coupling at such a short length scale. The RDF data also showed that the decay to a probability of 1 occurred at very long distances, somewhat longer than expected. These distances were still consistent with the concept of preferential accumulation of droplets occurring over the entire inertial range and the overall averages only being recovered at distances comparable to the integral length scale of the turbulence, which corresponds to approximately $2{,}000\eta$ in our experiments.

Our results provide quantitative experimental data on the RDF, albeit one dimensional, for inertial droplet interactions with high Reynolds number turbulence in a well-characterized canonical flow. We observe the importance of droplet–droplet interactions at short separations and the strong influence of these interactions in setting the RDF and, therefore, the collision rates. We also observe the influence of scale separation in this relatively high Re_λ laboratory turbulence. These RDF statistics can be used to validate DNS of similar droplet- or particle-laden flows and to compare against other data sets in the formulation of turbulence-induced collision kernels for small inertial droplets.

References

Albrecht H (2003) Laser Doppler and phase Doppler measurement techniques. Experimental fluid mechanics. Springer, Berlin

Aliseda A, Hainaux F, Cartellier A, Lasheras J (2002) Effect of preferential concentration on the settling velocity of heavy particles in homogeneous isotropic turbulence. J Fluid Mech 468:77–105

Arenberg D (1939) Turbulence as the major factor in the growth of cloud drops. Bull Am Meteorol Soc 20:444–448

Ayala O, Rosa B, Wang L, Grabowski WW (2008) Effects of turbulence on the geometric collision rate of sedimenting droplets. Part 1. Results from direct numerical simulation. New J Phys 10:075015

Bachalo W (1994) Experimental methods in multiphase flows. Int J Multiph Flow 20(Suppl):261–295

Bateson CP (2010) The radial distribution function as a quantication of the preferential concentration of cloud droplets in a turbulent flow. Master's thesis, University of Washington

Corrsin S (1963) Turbulence: experimental methods. In: Flugge S, Truesdall C (eds) Handbuch der Physik, vol VIII, Springer, Berlin, pp 524–590

de Almeida FC (1976) The collision problem of cloud droplets moving in a turbulent environment. Part I: a method of solution. J Atmos Sci 33:1571–1578

de Almeida FC (1979) The collision problem of cloud droplets moving in a turbulent environment. Part II: turbulent collision efficiencies. J Atmos Sci 36:1564–1576

de Almeida FC (1979) The effects of small-scale turbulent motions on the growth of a cloud droplet spectrum. J Atmos Sci 36: 1557–1563

East T, Marshall J (1954) Turbulence in clouds as a factor in precipitation. Q J R Meteorol Soc 80:26–47

Eaton J, Fessler J (1994) Preferential concentration of particles by turbulence. Int J Multiph Flow 20(Suppl):169–209

Faeth G, Hsiang LP, Wu PK (1995) Structure and breakup properties of sprays. Int J Multiphase Flow 21(Suppl):99–127

George W, Beuther P, Lumley J (1978) Processing of random signals. In: Hansen BW (ed) Proceedings of the dynamic flow conference on dynamic measurements in unsteady flows, Marseille, France and Baltimore, USA, pp 757–800

Goldstein, R (eds) (1996) Fluid mechanics measurements. 2nd edn. Taylor & Francis, Washington, D.C

Grover S, Pruppacher HR (1985) The effect of vertical turbulent fluctuations in the atmosphere on the collection of aerosol particles by cloud drops. J Atmos Sci 42:2305–2318

Gad-el Hak M, Corrsin S (1974) Measurements of the nearly isotropic turbulence behind a uniform jet grid. J Fluid Mech 62(part 1):115–143

Holtzer G, Collins L (2002) Relationship between the intrinsic radial distribution function for an isotropic field of particles and lower-dimensional measurements. J Fluid Mech 459:93–102

Jonas P (1996) Turbulence and cloud microphysics. Atmos Res 40:283–306

King L (1914) On the convection of heat from small cylinders in a stream of fluid: determination of the convection constants of small platinum wires with applications to hot-wire anemometry. Phys Fluids 214:373–432

Langmuir I (1948) The production of rain by a chain reaction in cumulus clouds at temperatures above freezing. J Atmos Sci 5(5):175–192

Lázaro BJ, Lasheras J (1992) Particle dispersion in the developing free shear layer. Part 1. Unforced flow. J Fluid Mech 235:143–178

Lumley J (1965) Interpretation of time spectra measured in high-intensity shear flows. Phys Fluids 8(6):1056–1062

Maxey M (1987) The gravitational settling of aerosol particles in homogeneous turbulence and random flow fields. J Fluid Mech 174:441–465

Maxey M, Corrsin S (1986) Gravitational settling of aerosol particles in randomly oriented cellular flows. J Atmos Sci 43:1112–1134

Maxey M, Riley J (1983) Equation of motion for a small rigid sphere in a nonuniform flow. Phys Fluids 26(4):883–889

Pinsky M, Khain A, Shapiro M (1997) Turbulence effects on droplet growth and size distribution in clouds—a review. J Aerosol Sci 28:1177–1214

Pinsky M, Khain A, Shapiro M (1999) Collisions of small drops in a turbulent flow. Part I: collision efficiency. problem formulation and preliminary results. J Atmos Sci 56(15):2585–2600

Pinsky M, Khain A, Shapiro M (2000) Stochastic effects of cloud droplet hydrodynamic interaction in a turbulent flow. Atmos Res 53:131–169

Pinsky M, Khain A, Grits B (2006) Collisions of small drops in a turbulent flow. Part III: relative droplet fluxes and swept volumes. J Atmos Sci 63(8):2123–2139

Pope S (2006) Turbulent flows. 2nd edn. Cambridge University Press, Cambridge

Reade WC, Collins LR (2000) Effect of preferential concentration on turbulent collision rates. Phys Fluids 12(10):2530–2540

Reuter GW, de Villiers R, Yavin Y (1988) The collection kernel for two falling cloud drops subjected to random perturbations in a turbulent air flow: a stochastic model. J Atmospher Sci 45:765–773

Reuter GW, Wright CJ, Eyre D (1989) Effects of turbulence on the growth of a cloud drop spectrum. J Atmos Sci 46:1407–1410

Rogers RR, Yau MK (1989) A short course in cloud physics. 3rd edn. Butterworth-Heinemann, Oxford

Ruger M, Hohmann S, Sommerfeld M, Kohnen G (2000) Euler/Lagrange calculations of turbulent sprays: the effect of droplet collisions and coalescence. At Spray 10:47–81

Saffman P, Turner J (1956) On the collision of drops in turbulent clouds. J Fluid Mech 1:16–30

Seifert A, Beheng K (2006) A two-moment cloud microphysics parameterization for mixed-phase clouds. Part 1: model description. Meteorol Atmos Phys 92(1-1):45–66

Shaw R (2003) Particle-turbulence interactions in atmospheric clouds. Ann Rev Fluid Mech 35:183–227

Shaw R, Reade WC, Collins LR, Verlinde J (1998) Preferential concentration of cloud droplets by turbulence: effects on the early evolution of cumulus cloud droplet spectra. J Atmos Sci 55:1965–1976

Squires K, Eaton J (1991) Preferential concentration of particles by turbulence. Phys Fluids 3(5):1169–1178

Sundaram S, Collins L (1997) Collision statistics in an isotropic particle-laden turbulent suspension. Part 1. Direct numerical simulations. J Fluid Mech 335:75–109

Taylor G (1938) The spectrum of turbulence. Proc R Soc Lond A 164(919):476–490

Truesdell G, Elghobashi S (1994) On the two way interaction between homogeneous turbulence and dispersed solid particles. II. Particle dispersion. Phys Fluids 6(3):1405–1407

Vaillancourt PA, Yau MK (2000) Review of particle-turbulence interactions and consequences for cloud physics. Bull Am Meteorol Soc 81:285–298

Vohl O, Mitra S, Wurzler S, Pruppacher H (1999) A wind tunnel study of the effects of turbulence on the growth of cloud drops by collision and coalescence. J Atmos Sci 56(24):4088–4099

Wang B, Xu D, Chu K, Yu A (2006) Numerical study of gas-solid flow in a cyclone separator. Appl Math Model 30(11):1326–1342

Wang L, Maxey M (1993) Settling velocity and concentration distribution of heavy particles in homogeneous isotropic turbulence. J Fluid Mech 256:27–68

Wang L, Wexler A, Zhou Y (2000) Statistical mechanical description and modelling of turbulent collision of inertial particles. J Fluid Mech 415:117–153

Wang L, Ayala O, Kasprzak S, Grabowski W (2005) Theoretical formulation of collision rate and collision efficiency of hydrodynamically interacting cloud droplets in turbulent atmosphere. J Atmos Sci 62(7):2433–2450

Wang L, Xue Y, Ayala O, Grabowski W (2006) Effects of stochastic coalescence and air turbulence on the size distribution of cloud droplets. Atmos Res 82:416–432

Wang L, Ayala O, Rosa B, Grabowski WW (2008) Turbulent collision efficiency of heavy particles relevant to cloud droplets. New J Phys 10:075013

Wells M, Stock D (1983) The effect of crossing trajectories on the dispersion of particles in a turbulent flow. J Fluid Mech 136:31–62

Xue Y, Wang L, Grabowski W (2008) Growth of cloud droplets by turbulent collision-coalescence. J Atmos Sci 65(2):331–356

Yaxin, Su (2006) The turbulent characteristics of the gassolid suspension in a square cyclone separator. Chem Eng Sci 61(5):1395–1400

Zaichik L, Alipchenkov V, Avetissian A (2006) Modelling turbulent collision rates of inertial particles. Int J Heat Fl Flow 27(5):937–944

Zhou Y, Wexler A, Wang L (2001) Modelling turbulent collision of bidisperse inertial particles. J Fluid Mech 433:77–104